LA-UR-23-22835

Approved for public release; distribution is unlimited.

Title: Density Measurement of NaCl-MgCl2-PuCl3 and NaCl-UCl3-PuCl3 Molten Salt Systems by Neutron Radiographic Dilatometry

Author(s): Parker, Stephen Scott
Long, Alexander Makenzie
Carver, Dale Travis
Jackson, Jay Matthew
Monreal, Marisa Jennifer

Intended for: Report

Issued: 2023-03-20

Density Measurement of $NaCl-MgCl_2-PuCl_3$ and $NaCl-UCl_3-PuCl_3$ Molten Salt Systems by Neutron Radiographic Dilatometry

S. S. Parker[1]

A. M. Long[1]

T. D. Carver[1]

M. J. Jackson[1]

M. J. Monreal[2]

[1]Materials Science and Technology Division, Los Alamos National Laboratory
[2]Chemistry Division, Los Alamos National Laboratory

CONTENTS

LIST OF TABLES

LIST OF FIGURES

Figure 14: Density of NaCl + UCl_3 + $PuCl_3$ samples as a function of temperature: (*top*) *0.317* NaCl + *0.663* UCl_3 + *0.02* $PuCl_3$ (*bottom*) *0.305* NaCl + *0.663* UCl_3 + *0.01* $PuCl_3$.

Figure 15: Calculated density of $PuCl_3$ as a function of temperature up to 1100 K, with extrapolation to 1300 K. Error bars represent 10% uncertainty. In the temperature range below the melt point of $PuCl_3$ ($T_m \approx 1040\ K$), the apparent density is only applicable above the liquidous temperature of multi-component systems containing $PuCl_3$.

Figure 16: Calculated density of $PuCl_3$ in $(NaCl+MgCl_2)_{eutectic}$ (blue) and $(NaCl+UCl_3)_{eutectic}$ (black) mixtures as a function of mol fraction additions of $PuCl_3$, plotted at $T = 1100\ K$.

Figure 17: (*left*) Phase diagram of NaCl, $MgCl_2$, and $PuCl_3$ at the calculated eutectic temperature. [14] Liquidous temperatures are given in kelvin and are indicated on the plot and are illustrated across the phase space with colored contour lines. (*right*) Phase diagram of NaCl, UCl_3, and $PuCl_3$ at the calculated eutectic temperature. [15]. Liquidous temperatures are given in degrees Celsius and are indicated on the plot by the color heat map given on the right.

EXECUTIVE SUMMARY

A novel neutron radiographic technique was developed and implemented to measure the change in volume as a function of temperature of select plutonium-containing liquid chloride mixtures from melt to 1250 K. These measurements were performed at Los Alamos National Laboratory by members of the molten salt research group under support from Gateway for Accelerated Innovation in Nuclear (GAIN) voucher NE-21-25117: "Density Measurements of Plutonium Bearing Salts via Neutron Beam Dilatometry". This technical report contains a description of the experimental method and a summary of the results. Initial characterization of the {NaCl, $MgCl_2$, UCl_3, $PuCl_3$} salts used in this experiment includes a combination of x-ray diffraction, differential scanning calorimetry, gamma ray spectroscopy, and inductively coupled plasma mass spectrometry. Four samples of NaCl + $MgCl_2$ + x *mol*% $PuCl_3$ and four samples of NaCl + UCl_3 + x *mol*% $PuCl_3$ were prepared at the Plutonium Facility, shipped to the Los Alamos Neutron Science Center (LANSCE), and radiographed with the density via neutron radiography (DvNR) apparatus. Density data in the form of meniscus heights were recorded as a function of temperature. The results show a linear dependence of density with temperature and a third order polynomial dependence of density with composition as a function of $PuCl_3$ addition in the corresponding halide salt mixture. Additions of $PuCl_3$ result in a significant increase in density of the salt mixture and a slight reduction in the coefficient of volumetric expansion. These results represent a first measurement of the density of plutonium chloride salt mixtures and, in combination with additional measurements, may lead to a generalized description of the density of such salt systems for arbitrary compositions and temperature.

1. Introduction

This investigation centers on the characterization of liquid chloride salts for application as a fuel bearing coolant in a novel nuclear reactor design. The thermophysical properties and high-temperature stability of fused salts[1] have been the subject of intermittent study and review, with renewed interest in recent years in fluorides and chlorides for use in molten salt nuclear reactors. Ionic melts are sought for these applications because they exhibit: (i) a broad liquid temperature range, (ii) low vapor pressure in the liquid state (iii) suitable heat capacity and thermal conductivity for thermal storage or transfer purposes, and (iv) low viscosity. As a fuel-bearing salt in a nuclear reactor, chloride salts support fast spectrum reactor designs and may be tailored to reduce parasitic neutron capture. Ongoing research efforts at national laboratories, universities, and private companies target specific property measurements necessary for the design and licensing of molten salt reactors. Research in this area is especially important given the lack of reliable data in the available literature.

This work is intended to provide high-quality density data as a function of temperature and composition for NaCl-$MgCl_2$-$PuCl_3$ and NaCl-UCl_3-$PuCl_3$ molten salt systems. Measurements of the density of liquid chlorides were performed by neutron radiography of a sealed volumetric dilatometer. The apparatus was capable of measurements up to 1250 K with an imaging resolution of $\sim 50 \mu m$. The modular, compact design of the furnace and sample assembly minimized sample volume, optimized the necessary attenuation through the sample, and reduced neutron scatter on the furnace components. Sealed inner crucibles enabled measurement on air-sensitive, hazardous materials, and the use of secondary containment enabled rapid sample changes. The large, multi-zone furnace provided consistent heat across the sample assembly and doubled as a tertiary barrier. Coupling the resolution possible with neutron radiography and a large, thermally stable test environment, this technique may produce property data with high accuracy and precision.

Neutron radiography is a well-established technique for the nondestructive visualization of the interior of complex systems and is uniquely well-suited for interrogation of large systems and multi-layered components. The pulsed neutron beam available at the Lujan Center at the Los Alamos Neutron Science Center (LANSCE) was ideal for this experiment: spanning thermal to epithermal regimes, the neutron beam may be tailored for the specific needs of a given imaging setup, such as intensity, areal coverage, and divergence, via various collimation and flight path length setups. For the measurements described in this work, an intense neutron beam with low divergence and large areal coverage was required. In what follows, the method of neutron radiography for the measurement of volumetric changes of liquid chlorides is presented, and the data is summarized and discussed within the context of previous measurements and the available, published literature. This report concludes with a summary and roadmap of future work which may lead to a generalized description of the density of such salt systems for arbitrary compositions and temperature.

[1] Equivalent and interchangeable with ionic liquid, ionic melt, liquid chloride, or molten salt.

2. Material Characterization

High purity (>99.99%) chloride salts {NaCl, $MgCl_2$} were purchased from Sigma-Aldrich and subsequently dried by conventional vacuum furnace methods. The apparent effect of drying salts prior to measurement was apparent as a shift in the melt onset and peak; thus, relative moisture content across different process batches was inferred from such data. Drying the salts results in a reduction of water content to ~0.01 wt%, however any initial oxide or oxychloride impurities are expected to remain. It this study, such impurities under this threshold are tolerated and are not expected to impact the results, given the predominance of other sources of measurement error. UCl_3 and the NaCl+36 *mol*% $PuCl_3$ eutectic salt were studied as-received. Pictures of the as-received actinide salts are shown in **Figure 1**. The color of the UCl_3 and NaCl+36 *mol*% $PuCl_3$ eutectic salt are consistent with published literature [1-3]. UCl_3 received from Terrapower was synthesized from uranium metal by conversion to hydride (UH_3) and subsequent chlorination to UCl_3. The UCl_3 was shipped in a glass vessel which was taped shut. NaCl+36 *mol*% $PuCl_3$ eutectic salt was received from Idaho National Laboratory (INL), where the initial $PuCl_3$ was synthesized by chlorination by reaction with NH_4Cl and then mixed with dried NaCl. The NaCl+36 *mol*% $PuCl_3$ eutectic salt was shipped in welded stainless-steel tubes, which remained sealed until samples were mixed and loaded into the primary tubes for the experiment. All materials were stored and processed in inert, dry gloveboxes. Initial characterization of $PuCl_3$ by gamma spectroscopy and inductively coupled plasma mass spectrometry (ICP-MS) was carried out at INL, and the results are summarized in **Table 1**. From these measurements the plutonium concentration was estimated as $5.56 \cdot 10^5 \mu g/g$.

Figure 1: Photographs of (*left*) UCl_3 received from Terrapower, and (*right*) NaCl + 36 mol % $PuCl_3$ eutectic salt received from Idaho National Laboratory.

Table 1: Initial material characterization by (*left*) gamma spectroscopy, and (*right*) inductively coupled plasma mass spectrometry (ICP-MS).

Analyte	Activity $\mu Ci/g$
^{241}Am	$1.41 \cdot 10^4$
^{144}Ce/Pr	< 0.8
^{60}Co	< 0.07
^{134}Cs	< 0.07
^{137}Cs	< 0.07
^{154}Eu	< 0.1
^{155}Eu	< 0.4
^{54}Mn	< 0.06
^{239}Np	< 0.3
^{239}Pu	$2.51 \cdot 10^4$
^{237}Np / ^{233}Pa	< 0.5

^{241}Am uncertainty is 3%,
^{239}Pu uncertainty of 5%.

Analyte	Concentration $\mu g/g$	Uncertainty %
^{109}Ag	12	20
^{138}Ba	12	15
M/Z 107	13	15
M/Z 241	6040	5
M/Z 242	1960	5
^{237}Np	212	5
^{239}Pu	469000	5
^{240}Pu	91600	5
^{88}Sr	8	15
^{234}U	60	10
^{235}U	406	5
^{236}U	283	5
^{238}U	246	5

Confirmation of bulk purity was carried out by x-ray powder diffraction (XRD) (D2 Phaser, Bragg-Brentano geometry, Ni-filtered Cu Kα, Bruker AXS, Karlsruhe, Germany), with comparison to available reference crystallographic data from the powder diffraction file (PDF-4+) database for NaCl, $MgCl_2$, and UCl_3, with planned measurement of the NaCl+36 *mol*% $PuCl_3$ eutectic salt in 2023. XRD is limited to the detection of gross impurities in excess of 1-2 wt%. All samples were prepared in an inert argon atmosphere dry box. XRD samples were sealed in the inert box. The powder was spread on a thin layer of vacuum grease on a low background silicon stage and sealed with a plastic dome which was transparent to x-rays; these sealed samples were transported and measured under inert atmosphere. The samples were scanned from $10 \leq 2\theta \leq 90$ over 6 hours. A second set of scans were taken immediately after the first scan in order to confirm that the seal remained intact throughout the measurement and no appreciable oxidation occurred. The background subtracted x-ray diffraction patterns of NaCl, $MgCl_2$, and UCl_3 are shown in **Figure 2** with the appropriate reference peaks from the PDF database.

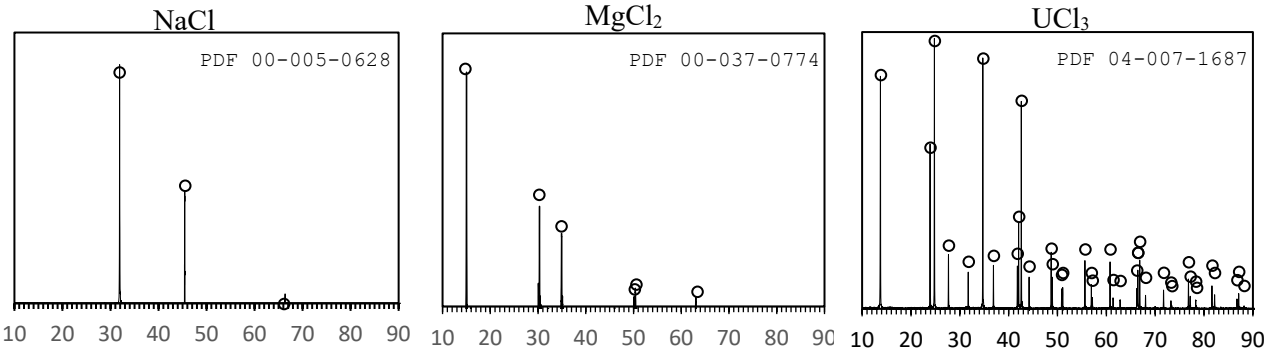

Figure 2: Background subtracted x-ray diffraction patterns of NaCl, $MgCl_2$, and UCl_3 from $10 \leq 2\theta \leq 90$. Reference peaks from the PDF database are plotted as (◦). Relative peak intensity and position closely match the PDF data.

Melt point and enthalpy of fusion measurements were performed with a differential scanning calorimeter (DSC) (Pegasus 404C, Netzsch Instruments, Germany) equipped with a rhodium-platinum high temperature furnace and type-K platinum sensor assembly. Samples were tested in sealed in commercially available CrNi steel (AISI 316L) crucibles using crush-seal gold or nickel foils, as shown in **Figure 3**. Alumina (Al_2O_3) liners were implemented in instances of material incompatibility between the sample and the crucible. Samples were sealed to 1-5 mN force with a specialized torque wrench. An upper test limit of 1300 K was chosen based on limitations of performance of the nickel sealing disk. Consistent with ASTM Standard E967, a five-point temperature calibration curve was created prior to testing using the following high purity standards: In, $KClO_4$, Ag_2SO_4, $BaCO_3$, and Ag. A separate set of calibrations are required for each crucible configuration. Proteus® analytical software (Netzsch Instruments, Germany) was used to determine the melt temperature by the extrapolated onset measurement on the instantaneous derivative of the measured $\mu V/mg$ signal. Following the procedure in ASTM standard E968, Proteus® analytical software was used to determine the sensitivity calibration curve from the observed change in enthalpy by integration of the signal generated during melt point measurements.

Figure 4 and **Figure 5** show the DSC thermograms of NaCl, $MgCl_2$, UCl_3, $PuCl_3$, and NaCl + 36 mol % $PuCl_3$ eutectic salt. Notable features include (1.) a consistent return to baseline, (2.) a sharp onset of a single peak, and (3.) a smooth derivative with no secondary events. The melt onset, melt peak, and the enthalpy of fusion are indicated on the plots and are consistent with reported literature. Melt point measurements were conducted at 10 K/min with the exception of the eutectic salt, which was measured with a heating rate of 20 K/min.

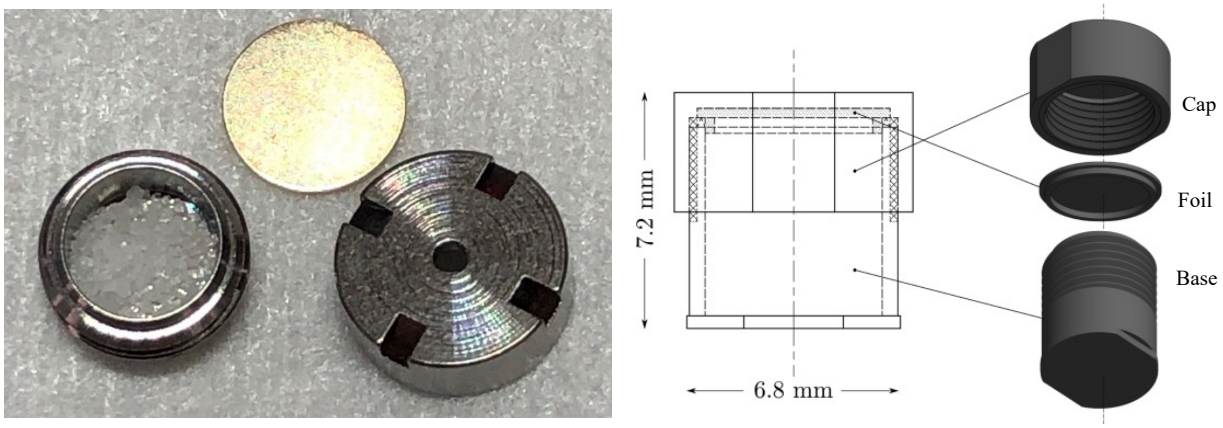

Figure 3: (*left*) Photograph of an unassembled stainless steel sealed crucible. A representative 20mg sample of NaCl is shown in the lower assembly on the left. (*right*) A schematic representation of a sealed DSC crucible. The order of assembly is shown.

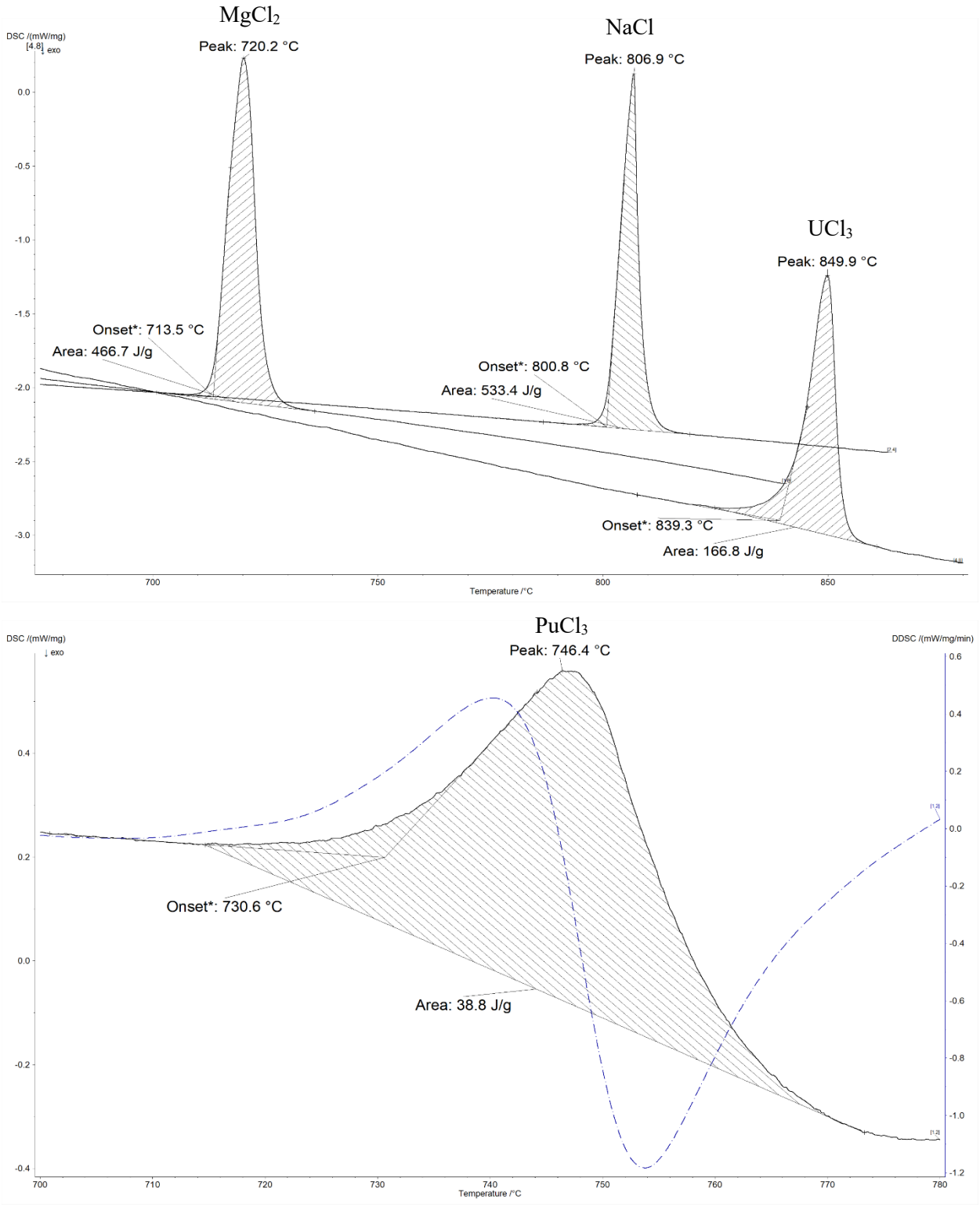

Figure 4: Differential scanning calorimetry thermograms of (*top*) NaCl, $MgCl_2$, and UCl_3; (*bottom*). $PuCl_3$. The blue dashed line is the first derivative.

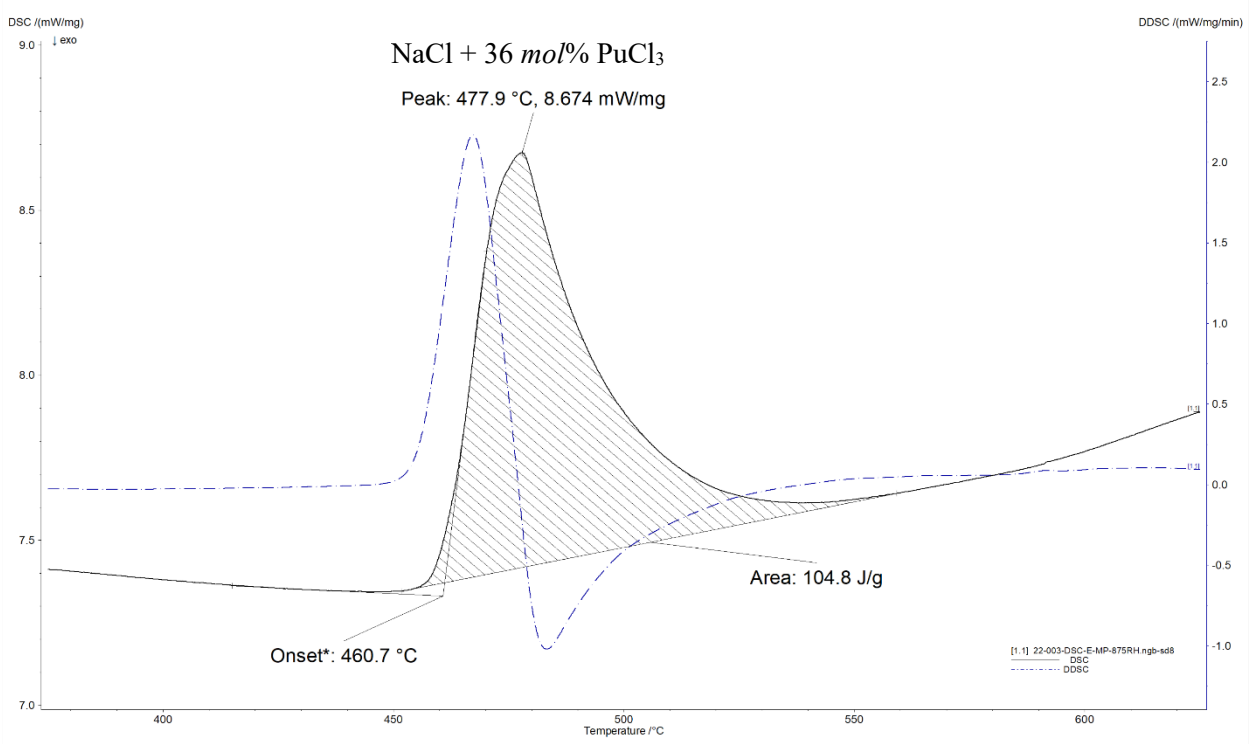

Figure 5: Differential scanning calorimetry thermogram of NaCl + 36 mol % $PuCl_3$ eutectic salt. The blue dashed line is the first derivative.

Experimental results from this study are reported as both the extrapolated onset and the peak melt in order to allow comparison with prior studies in which such a distinction is not always clear; this ambiguity may lead to differences of several degree Kelvin in reported melting points. The data is summarized in **Table 2**, with select references for comparison. Some of this variation may certainly result from the presence of impurities or by differences in composition of mixed samples.

Table 2: Measured melt point (onset and peak) and enthalpy of fusion data with comparison to select references.

Material	T_{onset} [K]	T_{peak} [K]	ΔH_{fusion}	Reference
NaCl	1070.7 ± 0.2	1076.6 ± 0.3	29 ± 1	This work
	1073.8‡	-	28.2	[7]
	1073.9‡	-	28.1	[8]
	1073‡	-	27.99 ± 0.06	[9]
	1073 ± 2‡	-	28.16 ± 0.14	[10]
$MgCl_2$	978.5 ± 0.1	986.8 ± 0.1	44 ± 1	This work
	987	-	43.1	[11]
	987	-	43.0	[8]
	987	-	43.2	[12]
	987 ± 2	-	43.1 ± 0.2	[10]
UCl_3	1108.2 ± 0.1	1116.2 ± 0.1	44 ± 1	This work
	1110	-	46.4	[7]
	1115 ± 2	-	49 ± 2	[13]
$PuCl_3$	734 ± 2	751 ± 2	105 J/g	This work
	726 ± 8*	-	-	[4]
	729 ± 5	753 ± 3	##	[5]
NaCl+ $PuCl_3$	460 ± 2	478 ± 2	105 J/g	This work
	### ± 8	### ± 3	##	[5]

‡Measurement not specified as onset or peak. Optical methods, employed by most reference, may report a delayed onset.
*Cooling Onset
** For a more comprehensive list of melt point data, see [6.].

3. Density Measurement by Neutron Radiographic Dilatometry

Density via Neutron Radiography measurements were conducted on the Flight Path 5 (FP5) beamline at the Los Alamos Neutron Science Center (LANSCE). FP5 is located at the Lujan Center which is a highly pulsed spallation neutron source that offers moderated neutron beams ranging from cold ($E_n < 25\ MeV$) to epithermal ($E_n > 1\ eV$). The main experimental cave for FP5 is located roughly 7 meters from a high intensity room-temperature water moderator on the 1L spallation target at the Lujan Center and therefore offers access to high flux thermal neutron beam for neutron imaging. The use of thermal neutrons for imaging on FP5 was chosen because neutrons at these energies are an ideal probe due to their high penetrability's through large amounts of most materials. DvNR measurements on eight $PuCl_3$-based salt samples were performed on FP5 during the LANSCE 2022 run cycle. The full setup on FP5 for these measurements is shown in **Figure 6**. Here moderated neutrons from the 1L spallation source impinged upon the apparatus. The imaging camera was located directly downstream of the furnace setup.

The apparatus consisted of sets of two orbitally welded 304 stainless steel Swagelok tubes held in place by a central reference guide, all of which was encapsulated in a conflat-sealed secondary container. This double containment strategy provided the safety basis for shipment and testing plutonium-containing salts. A single secondary container could insert into the compact, thin-walled furnace, and numerous secondary containers could be swapped out rapidly for high measurement throughput. The furnace assembly was positioned on a gantry which moved the sample in the plane orthogonal to the beam path. This control of sample position allowed for automated scripts to control the sample position and thereby generate series of overlapping radiographs covering the entire height of the sample tubes. Individual radiographs were complete on the order of minutes, however the total measurement time for a sample set depended on the thermal response of the furnace, which was optimized through a multi-zone design. A complete dataset could be collected in 12 hours, assuming sufficient beam quality. The following sections elaborate the method of sample preparation and the design of the experimental setup.

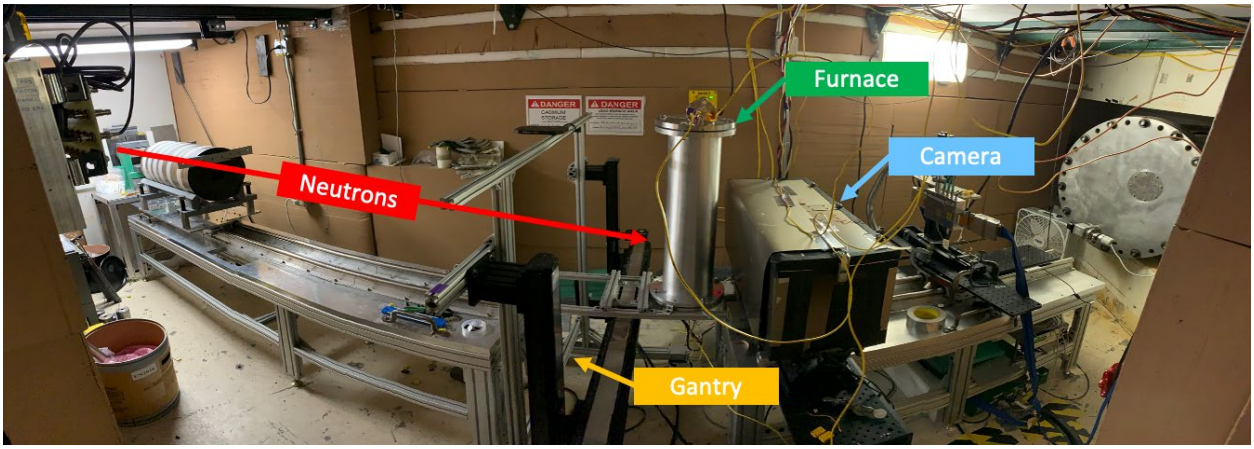

Figure 6. Panoramic view of the DvNR setup on FP5 during the measurements of $PuCl_3$-based molten salts. From left to right, the neutron beam (red) comes from the moderator source located on the 1L spallation target and enters the experimental cave at FP5. After passing through some final scraping collimation, the neutron beam impinges upon the furnace and molten salt samples that is loaded onto a motion gantry to allow movement of the setup in and out of the beam. Directly downstream of the furnace is the imaging setup that captures high resolution neutron radiographs of the molten samples.

3.1 Method

Sample Preparation, Primary Sample Tubes and Secondary Containment

The sample tubes were fabricated from 0.250" (6.35 mm) outer diameter 304 stainless steel tubing with a wall thickness of 0.049" (1.24 mm). The lower endcap, which consisted of a 0.62" (15.75 mm) length rod, was orbitally welded to the bottom of the sample tube and a ¼" tube plug was installed to seal the sample material. Example sample tubes are shown in **Figures 8**, **11**, and **12**. Prior to loading the sample material, all tubes were weighed while (1.) empty and (2.) filled with deionized water at 22 °C. The scale was calibrated to the appropriate range with check weights prior to use. Water was added to the tubes until a flat meniscus was achieved. The interior height of each tube was measured with a thin, inflexible tungsten wire and a caliper (+/- 0.04 mm) (Series 505, Mitutoyo, Tokyo, Japan). From the tube inner height and the water volume, the individual and average radii of the tubes were determined.

Salt mixtures were prepared in an inert argon atmosphere glovebox by measurement of additions of {NaCl, $MgCl_2$, UCl_3, or $(NaCl + PuCl_3)_{eutectic}$} into separate, interim vials. The vials were closed and rolled for 5 minutes to homogenize the sample. The sample was then poured into a clean weigh boat and then subsequently poured into the sample tube. The mass of the sample tube was measured while (1.) empty and (2.) filled with the salt sample. Once filled, the sample tubes were sealed with a ¼" Swagelok tube plug tightened to a measured gap of 0.135," as directed by the

manufacturer and verified with a no-go gap checker. The sample tubes were then passed out of the glovebox, decontaminated, loaded with the reference guide into the secondary containers, which was then loaded into a tertiary drum and shipped to LANSCE for radiography.

The sample matrix is given in **Table 3**. Sample masses were chosen so that the mixed composition would have a fluid column height of ~150 mm on melt. Pairs of duplicate sample compositions with nearly identical mass were tested together: the samples would melt simultaneously at the same composition, and equivalent mass resulted in the meniscus heights remaining within a single radiograph field of view throughout all measurements. Measuring duplicate samples also provided insight into the precision of the experiment. Varying the plutonium concentration between samples of the same salt system, allows estimation of the dependence of density on both composition and temperature. This is especially useful when estimating the impact of additions of arbitrary amounts of $PuCl_3$ in eutectic mixtures of the base salts.

Table 3: Sample matrix. Compositions are given in mol %.

Sample ID	NaCl	$MgCl_2$	UCl_3	$PuCl_3$	Mass [g]
1	41	53.3	-	5.7	4.736
2	41	53.3	-	5.7	4.766
3	40.3	57	-	2.7	4.691
4	40.3	57	-	2.7	4.675
5	31.7	-	66.3	2	7.007
6	31.7	-	66.3	2	6.945
7	30.5	-	68.5	1	7.002
8	30.5	-	68.5	1	7.029

The secondary containers consisted of 1.5” (38.1 *mm*) outer diameter, 0.065” (1.65 *mm*) wall thickness, 304 stainless steel tubing with a full penetration flush welded cap on one end and a welded 2 ¾” half nipple flange on the other. The flange was located out of the hot zone of the furnace; the temperature of this flange was monitored and interlocked to ensure that it did not exceed the maximum rated temperature of 450 °C, as established by the manufacturer. When heated from room temperature to 1200 K, the internal pressure of the secondary did not exceed 3 atm. The internal pressure of the primary and the secondary containers were equal throughout the measurement, and total anticipated change in pressure on a sample tube was calculated as < 0.014 *atm* based on the maximum expected thermal gradient across the secondary containment.

Furnace Design

A specialized compact furnace was designed and built for this experiment by the Neutron Scattering Science Team (NSST). Key design requirements for this furnace centered around need to have a close and unobstructed path between the samples and imaging plane of the detector, and the need for multiple levels of sample containment. Schematic representations of this furnace and the various levels of containment are shown in **Figure 7**. In this top-down cross-section view, the neutron beam enters from the top. The furnace coils (yellow) are set apart from the centerline on a 45 *mm* diameter ring centered around the sample containment. The heating elements azimuth placement allowed for a 25 mm viewing window unobstructed by heating elements. The furnace outer diameter was 150 mm. Initial designs required a 3" sample-to-image-plane distance and a 1" unobstructed field of view around the samples. This 1" unobstructed field of view was achieved by removing specific heating element coils that would otherwise clutter the imaging of the fluid meniscus. Custom heating assemblies (elements and insulation) were fabricated by Zircar Ceramics and delivered in June 2022.

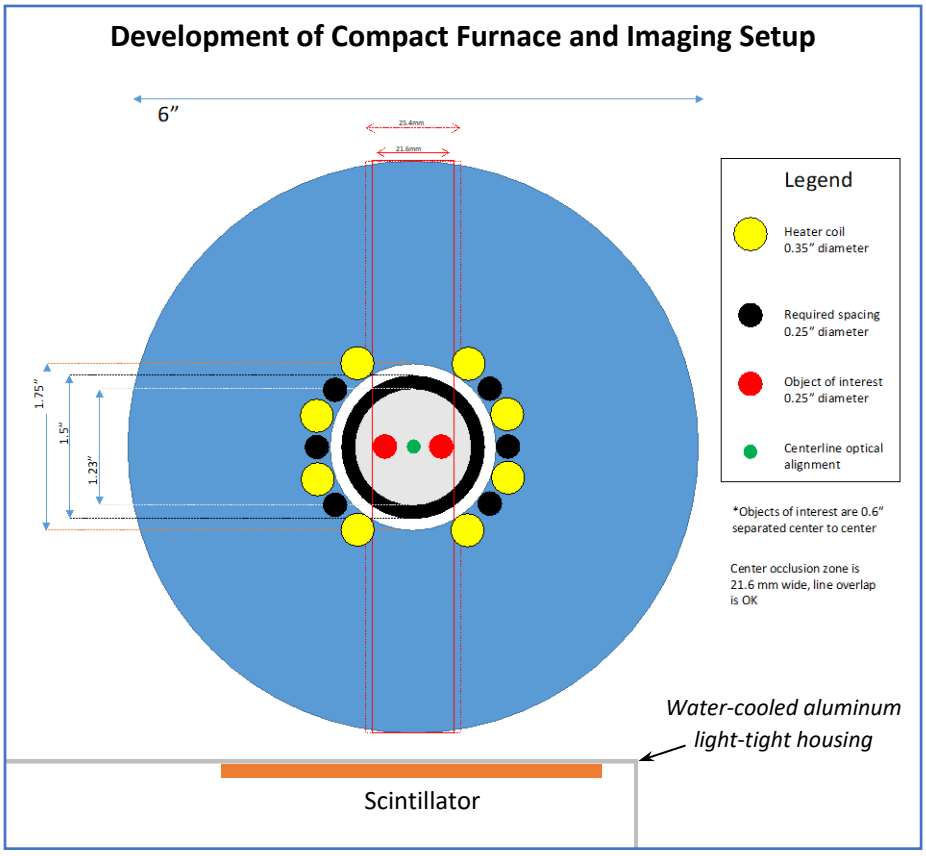

Figure 7: Schematic top-down cross section of the compact furnace and imaging setup.

In addition to optimizing the design for imaging, the test assembly required multiple levels of containment as per LANSCE safety operations guidelines, especially concerning heating plutonium-containing samples. The containment scheme is shown in **Figure 8**. The furnace shell acted as a tertiary layer of containment and was sealed on both ends by conflat flanges. The entire furnace is sealed within a 6" ID aluminum pipe with thermocouple, cover gas, and power feed throughs on either end. Nested within the center of the furnace is either a 1¼" quartz or steel tube that contains the sample assembly. The sample assembly consisted of a steel sample mount that acted as a reference guide and two orbitally welded, sealed 304 stainless steel Swagelok tubes. The full furnace assembly, once samples were loaded and sealed, was place on a Zaber Motion gantry that allowed for movement in and out of the beam remotely. All aspects of the furnace control, temperature readouts, interlocks, gantry position, and radiograph acquisition were controlled remotely and with a high degree of automation.

Several thermocouples were deployed at various containment levels to monitor temperatures of the capillary samples, the secondary containment flange, and the heating elements within the Zircar heater assemblies. Redundant element heater and interlock thermocouples passed through the conflat flanges via Type-K thermocouple nickel-chromium/nickel-aluminum pins. The furnace temperature feedback loop was read by a thermocouple embedded in the heating elements, and the compliance voltage on power supply was set to control maximum heater power at 1200 Watts, ~35% output, or 12.5 Volts. Sample temperature was read by a thermocouple suspended in the secondary containment alongside the primary tubes. The end of the sample thermocouple was located 70 mm from the base of the reference ruler, which coincided with the middle of the 150 mm fluid column height on melt of the samples. Given the strict safety operations envelope surrounding the heating of Pu samples, the maximum achievable temperature around the samples was limited by the maximum allowable temperature of the copper gasket located within the secondary conflat seal. This temperature was monitored and interlocked to a temperature controller (Lakeshore 336, Lake Shore Cryotronics, USA) set to an upper limit of 425 °C, which is below the temperature rating of 450 °C of the copper conflat seal.

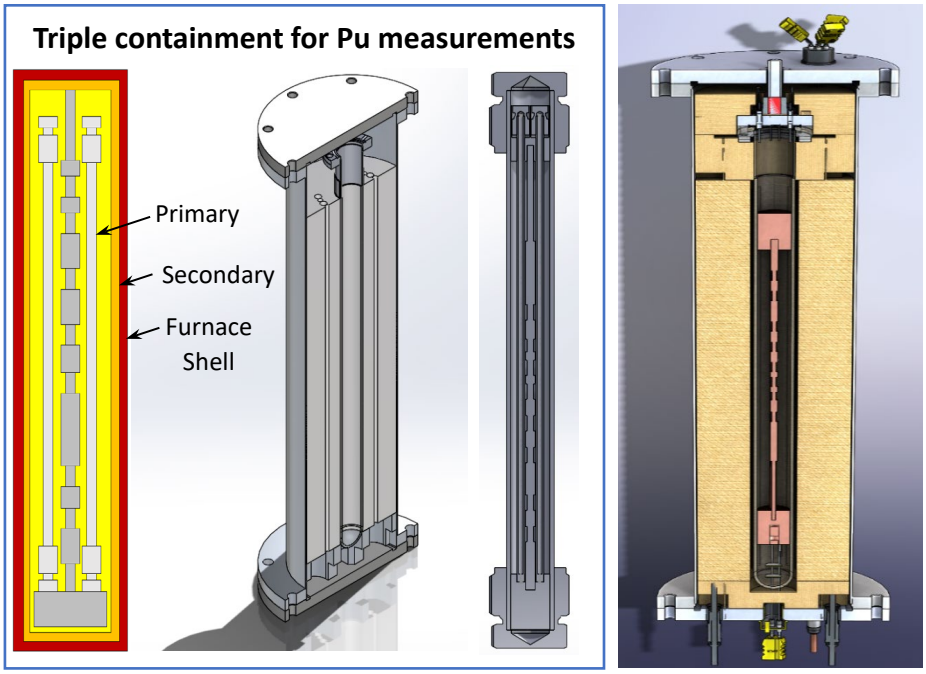

Figure 8: (*left*) Concept drawing of the containment scheme, along with CAD renders of the furnace assembly and a preliminary design of the assembled secondary and primary capsule. (*right*) Cross section of the assembled apparatus. This graphic captures the final design iteration, with key features such as thermocouple passthroughs and the furnace power supply.

Detector Design

A new imaging setup was designed and build using a 200 μm ZnS:LiF scintillator, 50mm lens (Milvus, ZEISS, Germany), and a high-speed high-resolution charge coupled device (CCD) astronomy camera (ASI2600mm, ZWO, Suzhou, China). All components of the detector were placed within a water-cooled aluminum light-tight housing. In this configuration, the imaging assembly could produce ~50 μm resolution images in < 1 minute exposures, which enables the production of movies of melt and solidification of the samples with 1 °C per minute ramp rate. With this imaging setup, neutron radiographs were recorded with the samples and furnace in and out of the beam, which allowed for transmission and neutron attenuation images to be calculated.

The field of view for the neutron detector was 90 x 90 mm, with a homogeneous illumination of the beam. The field of view was adequate to capture the reference and the meniscus position of the fluid in both sample tubes at any given temperature. The assembly of the reference with the two sample tubes was ~40cm in height. Therefore, 13 images were taken at various heights as the furnace was lowered through the neutron beam. Full composite images of the entire sample

assembly were obtained by stitching this series of images together. A minimum of 4 composite images of each pair of samples were taken at temperatures between room temperature and 1250 K. At each temperature step the apparatus stabilized for up to 1 hour prior to recording the radiographs. In between the temperature steps of the full composite images, the meniscus was continuously imaged with 1-minute radiographs. Thus, accurate determination of solution density as a function of temperature was achieved by measuring the location of the meniscus while simultaneously considering any important flaws or features which may impact the apparent volume of the fluid.

To obtain high quality neutron attenuation images for each sample pair, radiographs without the samples in the beam, known as "flat images", were recorded before and after samples were heated. Additionally, images without the beam, known as "dark images", were recorded periodically throughout the measurements to account for thermal back-ground noise in the CCD readout chip. Example radiographs of flats, darks, and samples images are shown in **Figure 9**. All radiographs and images were taken with a ZWO ASI2600mm camera and a 1 min exposure.

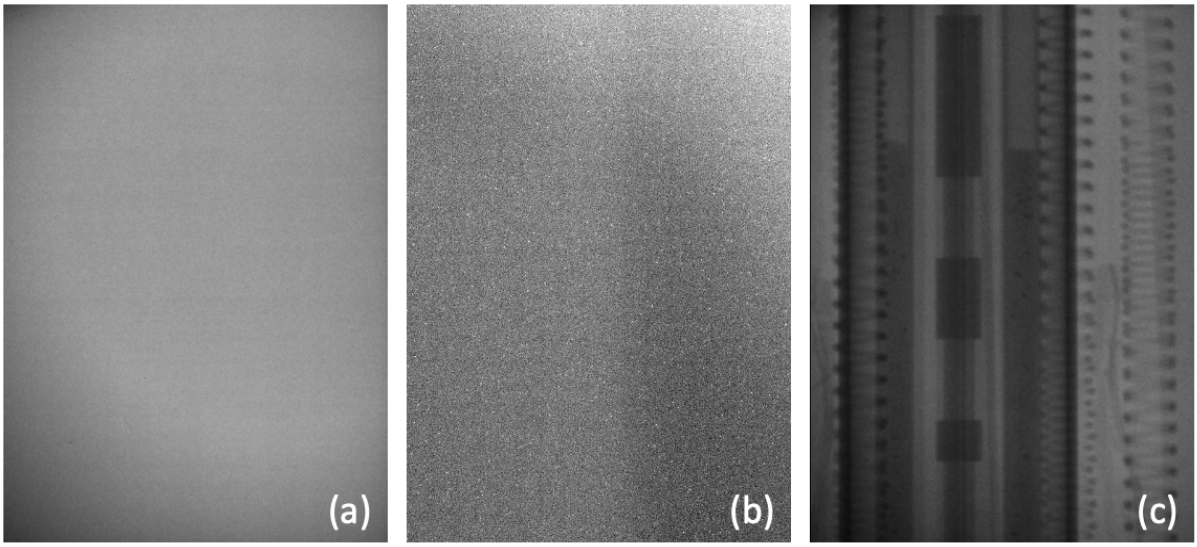

Figure 9. Example radiographs from a given sample. (a) A radiograph taken with no samples or the furnace in the beam. These are known as "flat field" images or $I_{flat}(x,y)$. (b) Images taken without beam, known as "dark field" images or $I_{dark}(x,y)$. These types of images account for background induced by thermal fluctuations in the CCD chip. (c) A radiograph of the samples and the furnace, $I_{sample}(x,y)$.

3.2 Analysis

Computing Neutron Attenuation Images:

Once all the sample radiographs, along with flat and dark images, were recorded neutron attenuation images were computed using the following equation,

$$Atten(x,y) = log\left[A_{norm}\frac{I_{sample}(x,y)-I_{dark}(x,y)}{I_{flat}(x,y)-I_{dark}(x,y)}\right].$$

Here, $I_{sample}(x,y)$ is the sample image, $I_{dark}(x,y)$ is the image without beam, $I_{flat}(x,y)$ is the radiograph with beam, but without the samples or furnace, and A_{norm} is the neutron beam normalization constant. Neutron attenuation images were generated using this equation for all raw sample radiographs recorded.

Determination of the Meniscus Height

Using neutron attenuation image for a given sample pair at a given temperature, meniscus heights were determined relative to the nearest feature on the reference by measurement of the greyscale values across features of the radiographs using the software ImageJ. Meniscus position and uncertainties were found by fitting error functions on the line profiles of the grey scale values as a function of pixel position. An example of this process is given in **Figure 10**. The scan direction is indicated on both the radiograph and the plot as red arrows. The meniscus is located at inflection point, and the relative uncertainty is given by a normalized gaussian which spans the change in grey scale value. Once the meniscus location is found in terms of a pixel position, the distance between the meniscus location and a feature on the reference guide was measured in terms of pixel number. The distance between any features on the reference guide are known, and so the difference in pixel position may be directly related to a known length. Therefore, the distance between the meniscus and the nearest reference feature is measured, which is then added or subtracted from the nearest height of a feature on the reference guide.

$$G.V. = A\ erf\left(\frac{x-x_o}{B\sqrt{2}}\right) - C\ x + D$$

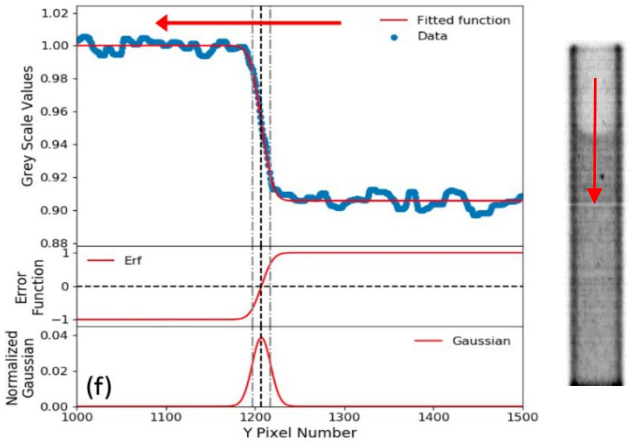

Figure 10: Grey scale value as a function of y-axis pixel number, scanned along the red arrow depicted on the radiograph on the right. The corresponding scan direction is indicated on the plot, and the fitted function is overlain on the data in red with the corresponding error function plotted below. The inflection point in these plots represents the boundary of the meniscus, and the normalized gaussian corresponds with the error in the pixel position of the inflection point.

See **Figure 11** (a.) and (b.) for the configuration of the sample tubes with the height reference guide. A motorized stage allowed precise movement of the furnace and attached experimental apparatus, which allowed composite images to be taken of the entire sample crucible. Using the reference as a guide for alignment, a set of radiographs along the height of the setup was stitched together into a single image. Images were cropped and line edges of notches were fitted with error functions plus first-order polynomial to determine the 50% crossing of the change in grey scale value. Once the same line edge was found in two adjacent images, the two images were stitched together with an averaged overlap region. This process was repeated until all five images were stitched together to yield an accurate composite of the full length of the setup. An example of the result of this process is shown in **Figure 11** (c.) for the case of samples 2 (*left*) and 3 (*right*) at 960 K. Considering the entire image, the alignment of the sample tubes with the reference and the relative rotation of the assembly with respect to the path of the beam are readily apparent. This composite image offers several advantages compared to merely imaging the meniscus. Three examples are shown in the blow-up sections next to the example radiograph: (*top*) In this instance, residual material remained on the inner wall of the crucibles when the samples melted. The volume of this material may be measured and accounted in the final analysis. (*middle*) The curvature and location of the meniscus are clearly identified. The field of view is sufficient to identify the height of the corresponding feature on the reference, given that the characteristic features to not repeat. (*bottom*) The curvature and location of the top of the orbitally welded endcap are evident. Separation of the primary tubes from the base of the reference is apparent and may be taken into account in the final analysis. While not shown in this radiograph, some samples may retain bubbles upon melt. The composite image may be used to identify bubbles: measuring the volume of the entrapped gas will factor into the density data for that sample.

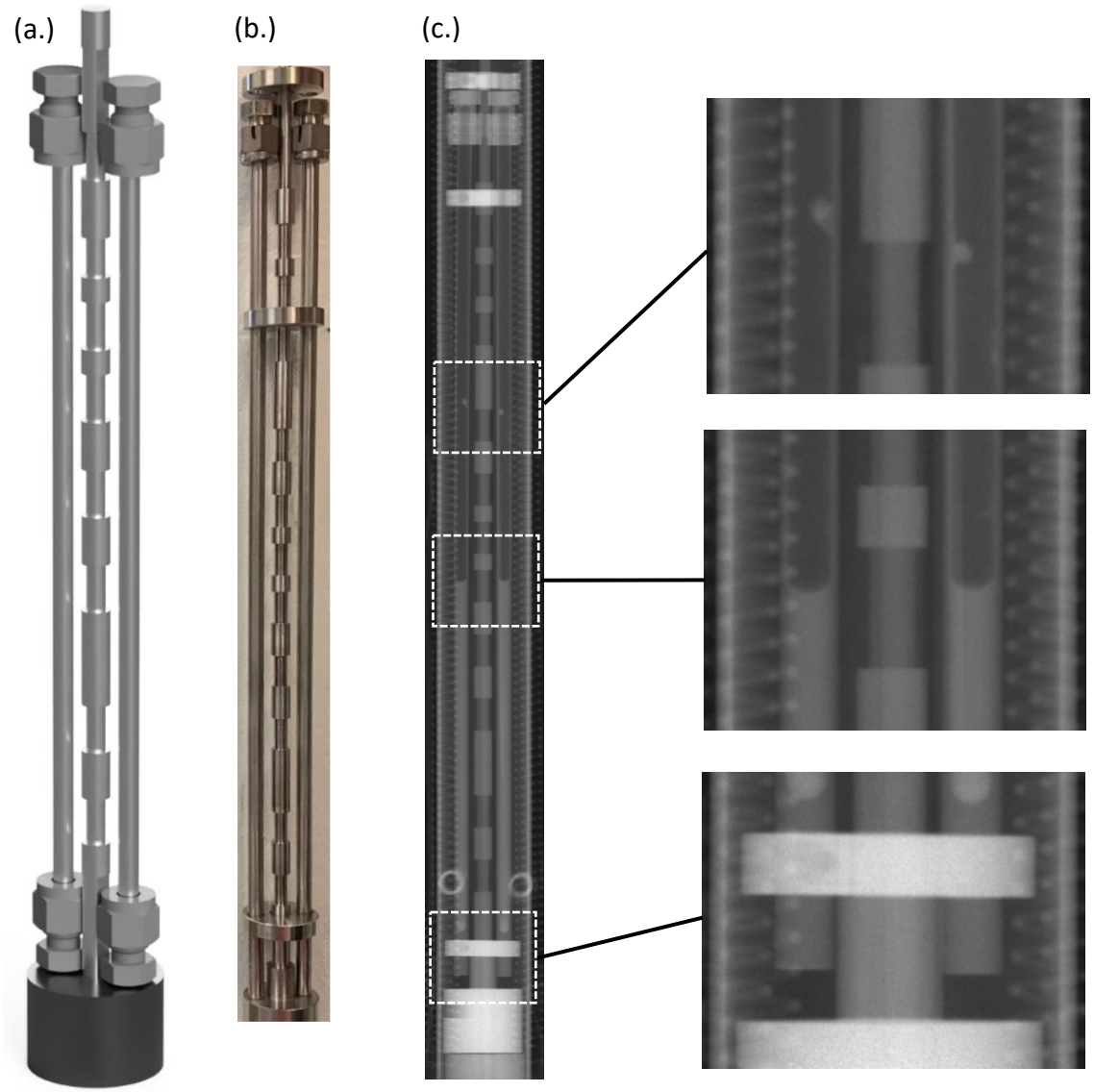

Figure 11: (a.) CAD render of the preliminary sample capsules alongside the reference ruler. (b.) Photograph of the final design of the sample tubes, shown attached to the reference ruler with circular spacers. The Swagelok base depicted in the CAD drawing was ultimately replaced with orbitally welded end caps, which significantly reduced geometric complexity (c.) Stitched neutron radiograph of the primary capsules alongside reference ruler. Blow-up cropped images of the radiograph highlight key features relevant to the analysis.

Coefficient of Expansion of the Sample Crucible and Reference Guide

A source of uncertainty arises from the thermal expansion of the sample crucible and the reference ruler. In the case of an expanding radius of the 304 stainless steel crucible, the inner diameter will expand by $(1 + \alpha_{316ss}(T) \cdot \Delta T)$. Given an initial inner radius of r_0, the inner radius at a given temperature is:

$$r(T) = r_0(1 + \alpha_{304ss}(T) \cdot \Delta T)$$

Accounting for thermal expansion of the reference guide, the meniscus height may be expressed in terms of the length of the 304ss reference ruler:

$$h(T) = l_0(1 + \alpha_{304ss}(T) \cdot \Delta T)$$

where h is the height of the reference, l_0 is the length of the reference at room temperature, and α_{304ss} is the coefficient of thermal expansion of the stainless steel. Characterization of the height as well as the diameter of the sample crucible due to thermal effects required measurement of the linear thermal expansion of the 304ss used in these components. A sample of 304ss, 30 mm long and 6 mm in diameter was tested in a conventional pushrod dilatometer from room temperature to 1300 K. From the instantaneous derivative of the change in length of the 304ss sample over the original 30 mm length of the sample (dL/L_0), the measured coefficient of thermal expansion, α_{304ss}, was found to be essentially constant across the temperature range relevant to the experiment ($600 \leq T \leq 1200\ K$):

$$\alpha_{304}(T) = 14.68 \cdot 10^{-5} + 3.5 \cdot 10^{-9} \cdot T$$

Thus, the expression for density of the liquid salt as a function of temperature, ρ(T), is:

$$\rho(T) = M \cdot \left(\pi[r_0(1 + \alpha_{316ss}(T) \cdot \Delta T)]^2 \cdot \left[l(1 + \alpha_{ref}(T) \cdot \Delta T)\right]\right)^{-1}$$

where M is the mass of the liquid, and l corresponds to the apparent height of the meniscus, in terms of the distance to the nearest known length feature on the reference ruler and the addition of that known length.

Bubbles and Abnormal Features

Bubbles within the liquid, material attached to the inner wall of the crucible and not in the melt, and any gap between the sample tube and the base of the reference guide will all impact the apparent volume of the liquid. These factors must be accounted for during analysis. Following the method for identifying the location of the meniscus, the diameter of bubbles and residual material are found by the inflection points in the greyscale values from line scans across the feature. The bubble/residue is approximated as spherical, and the relative error associated with the volume of that feature is propagated forward in the uncertainty calculation for that measurement. Gaps are recorded by direct measurement and are subtracted from the apparent meniscus height.

3.3 Error Propagation

The resolution of this method is limited by the performance of the camera and total attenuation of the signal through the furnace and sample containment. Uncertainty of a length measurement, Δx, is determined from the inflection in the change in grey scale value from a line of pixels across the meniscus: a pixel blur of $\Delta x = 5$ pixels (≈ 50 μm) is found to be the functional limit to determine the location of distinct features on the radiographs, and this error is expressed in the height uncertainty. The percent uncertainty in density is calculated by propagating forward sources of uncertainty in the camera resolution, temperature, geometry of the sample crucible, and any aberrant features. The temperature at test conditions was verified by a witness thermocouple 70 mm from the base of the reference guide, which was the approximate center of the liquid columns on melt. Following a change in temperature, the apparatus was set to an isothermal hold in order to establish thermal equilibrium prior to radiography. The temperature difference across the height of the sample tube is not expected to vary by more than $\Delta T = \pm 5$ K. This will be verified by follow on measurements of the furnace environment. The uncertainty in height due to temperature uncertainty is calculated from the thermal expansion of the reference and sample crucible (*see section 3.2*). Thus, error propagation is as follows:

$$\text{Height Uncertainty:} \quad \Delta h = \sqrt{(\Delta x)^2 + (\Delta L)^2}$$

$$\text{Volume Uncertainty:} \quad \Delta V = V\sqrt{2 \cdot \left(\frac{\Delta r}{r}\right)^2 + \left(\frac{\Delta h}{h}\right)^2}$$

$$\text{Density Uncertainty:} \quad \Delta \rho = \rho\sqrt{\left(\frac{\Delta M}{M}\right)^2 + 2 \cdot \left(\frac{\Delta r}{r}\right)^2 + \frac{(\Delta x)^2 + (\Delta L)^2}{h}}$$

where ΔL is the uncertainty in height of the nearest reference mark (50 μm), the uncertainty in mass is $\Delta m = 0.5$ mg, and the uncertainty in radius is $\Delta r = 8$ μm. The average radius of all tubes was determined to be 2.294 mm with $2\sigma = 10$ μm. The relationship between the uncertainty of density and meniscus height varies as $\Delta \rho \propto (1/h)^{1/2}$.

3.4 Data

Multiple neutron radiographs of the test chamber enable study of the fluid volume as a function of temperature. A set of images at the same temperature step may be stitched into a composite image, from which meniscus heights are recorded. A set of composite images constitute a complete dataset for two samples, as shown in **Figure 12** for *0.41* NaCl + *0.533* $MgCl_2$ + *0.057* $PuCl_3$ samples #1 and #2. The solid, uncompacted salt mixture is shown on the left in the room temperature image. Liquification of the sample is seen by a rapid consolidation of sample material, which is accompanied by a change in attenuation. View of the entire sample assembly allows identification of aberrant features, such as the gap between the sample tubes and the base of the reference guide or the apparent residual material which remains on the inner walls of the sample tubes throughout this experiment.

The density correlations of all samples are summarized in **Table 4**, and the {NaCl + $MgCl_2$ + $PuCl_3$} and {NaCl + UCl_3 + $PuCl_3$} data are plotted in **Figures 13** and **14**, respectively.

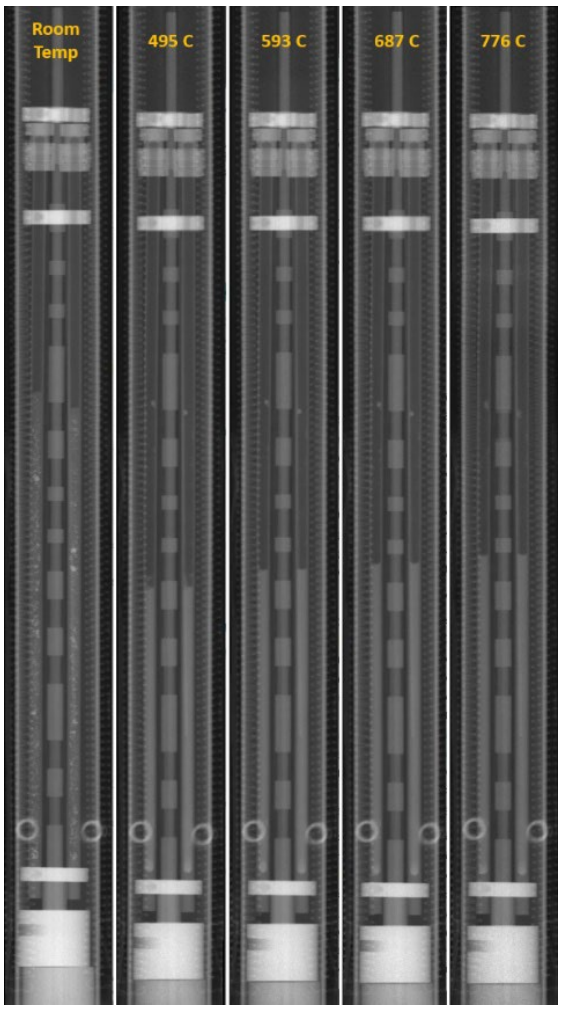

Figure 12: Progression of stitched radiographs of samples 1 and 2 from room temperature to 937 K.

Table 4: Fit parameters for density correlations for the ternary salt mixtures, of the form $\rho[g/cm^3] = \rho_0 - \alpha * T[K]$. Compositions are reported as mol fraction.

Ternary Mixtures	ρ_0 [g/cm^3]	$\alpha \cdot 10^{-3}$	Uncertainty	Range [K]
0.410 NaCl + *0.533* $MgCl_2$ + *0.057* $PuCl_3$	2.4538	0.6579	±0.02	823-960
	2.4681	0.6798	±0.02	
0.403 NaCl + *0.570* $MgCl_2$ + *0.027* $PuCl_3$	2.2732	0.6078	±0.01	913-1107
	2.2992	0.6401	±0.01	
0.317 NaCl + *0.663* UCl_3 + *0.020* $PuCl_3$	4.1099	1.0349	±0.02	941-1077
	4.1100	1.0345	±0.02	
0.305 NaCl + *0.685* UCl_3 + *0.010* $PuCl_3$	3.9360	0.8457	±0.04*	936-1075
	3.9245	0.8315	±0.05*	

*Additional uncertainty due to measurement of aberrant features: residue

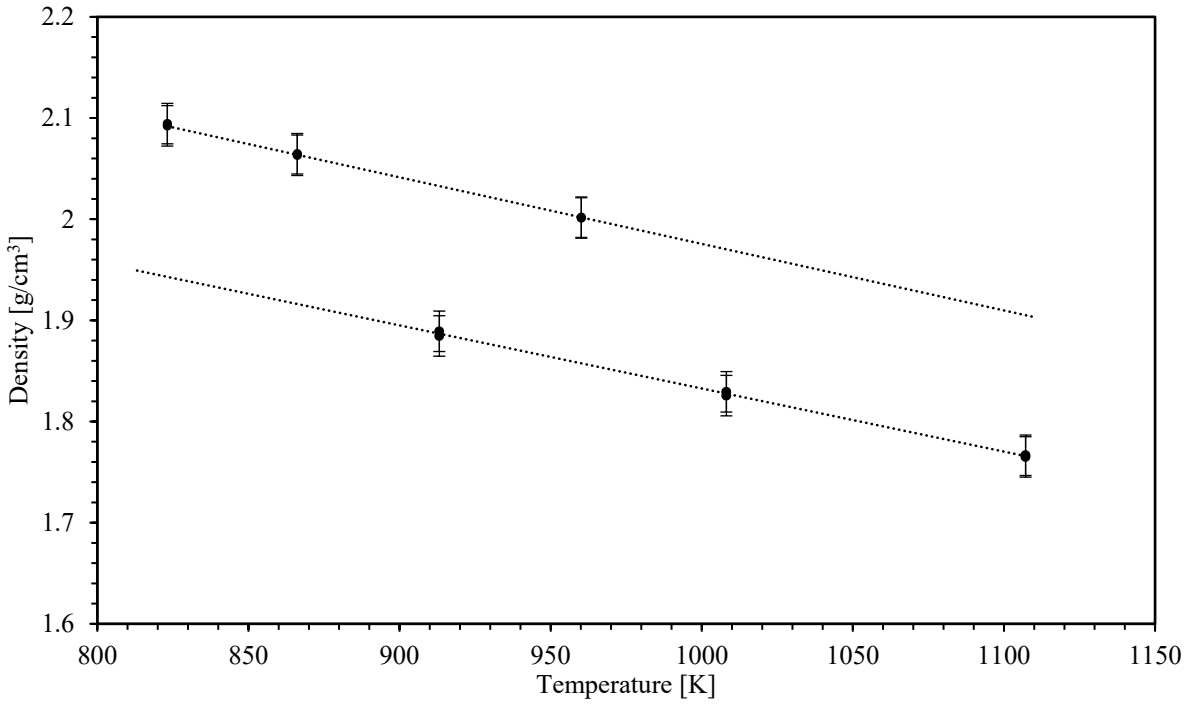

Figure 13: Density of NaCl + $MgCl_2$ + $PuCl_3$ samples as a function of temperature: (*top*) *0.41* NaCl + *0.533* $MgCl_2$ + *0.057* $PuCl_3$ (*bottom*) *0.403* NaCl + *0.57* $MgCl_2$ + *0.027* $PuCl_3$.

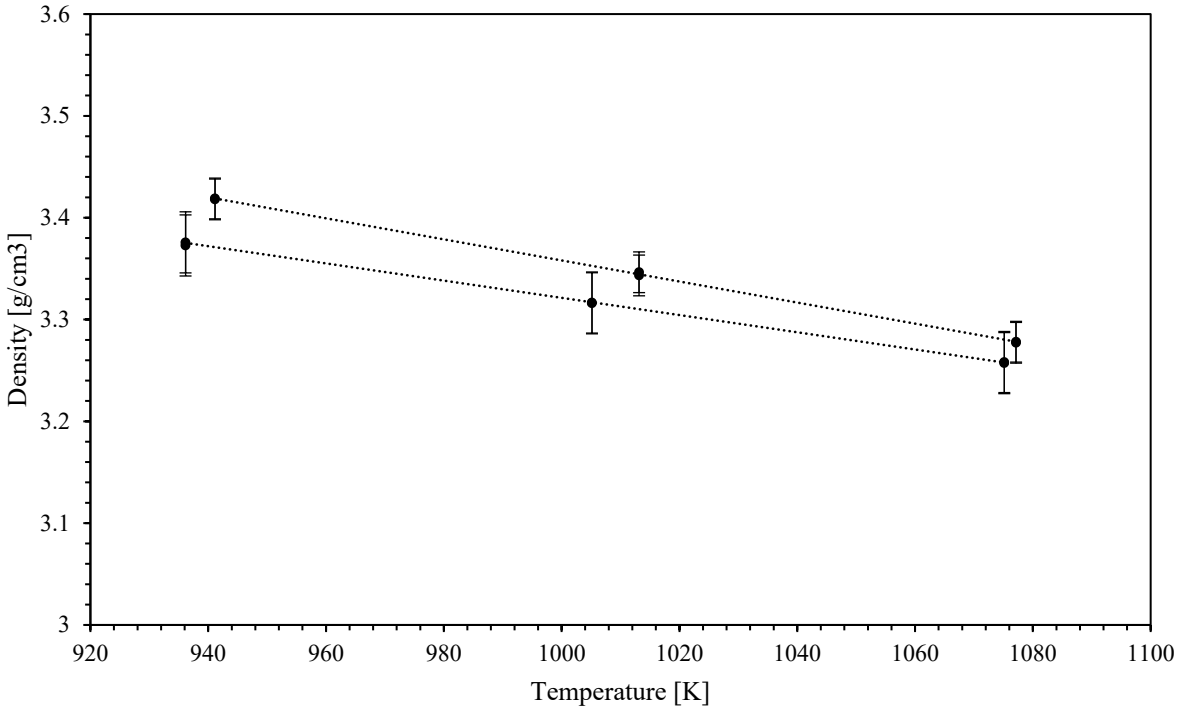

Figure 14: Density of NaCl + UCl_3 + $PuCl_3$ samples as a function of temperature: (*top*) *0.317* NaCl + *0.663* UCl_3 + *0.02* $PuCl_3$ (*bottom*) *0.305* NaCl + *0.663* UCl_3 + *0.01* $PuCl_3$.

Density as a Function of Composition

The density of the mixture of component A and B is:

$$\rho_{mix}(T) = f_{vol,\,A}(T) \cdot \rho_A(T) + f_{vol,\,B}(T) \cdot \rho_B(T)$$

where $f_{vol,\,i}(T)$ is the volume fraction of component *i* at temperature T. In terms of the mass fractions:

$$\rho_{mix}(T) = \frac{\rho_A(T) \cdot \rho_B(T)}{x_A \cdot \rho_B(T) + x_B \cdot \rho_A(T)}$$

where x_i is the mass fraction of component *i*. This expression of ρ_{mix} may also be stated in terms of mol fraction:

$$X_{mol,\,A} = \frac{(x_A/M_A)}{(x_A/M_A)+(x_B/M_B)} \qquad X_{mol,\,B} = \frac{(x_B/M_B)}{(x_A/M_A)+(x_B/M_B)}$$

where M_i is the molar mass component *i*.

For a mixture of components A and B in which the density of component A is not known, the density of that component may be calculated as:

$$\rho_A(T) = \frac{x_A \cdot \rho_{mix}(T) \cdot \rho_B(T)}{\rho_B(T) - (1 - x_A) \cdot \rho_{mix}(T)}$$

This method of estimation from two species also applies to a mixture of a component A added to a eutectic mixture, B+C, to make a ternary mixture, A+B+C:

$$\rho_A(T) = \frac{x_A \cdot \rho_{B+C}(T) \cdot \rho_{A+B+C}(T)}{\rho_{B+C}(T) - (1 - x_A) \cdot \rho_A(T)}$$

For an arbitrary mixture of components A, B, and C, the density of the mixture is:

$$\rho_{mix}(T) = \frac{\rho_A(T) \cdot \rho_B(T) \cdot \rho_C(T)}{x_A \cdot \rho_B(T) \cdot \rho_C(T) + x_B \cdot \rho_A(T) \cdot \rho_C(T) + x_c \cdot \rho_A(T) \cdot \rho_B(T)}$$

The density of component A may be determined from this expression as:

$$\rho_A(T) = \frac{x_A \cdot \rho_{mix}(T) \cdot \rho_B(T) \cdot \rho_C(T)}{\rho_B(T) \cdot \rho_C(T) - x_B \cdot \rho_{mix}(T) \cdot \rho_C(T) - x_c \cdot \rho_{mix}(T) \cdot \rho_B(T)}$$

Thus, the density of $PuCl_3$ as a function of temperature and composition may be determined from the data reported in **Figures 13** and **14**. The results of these calculations are summarized in **Figure 15** and **16**.

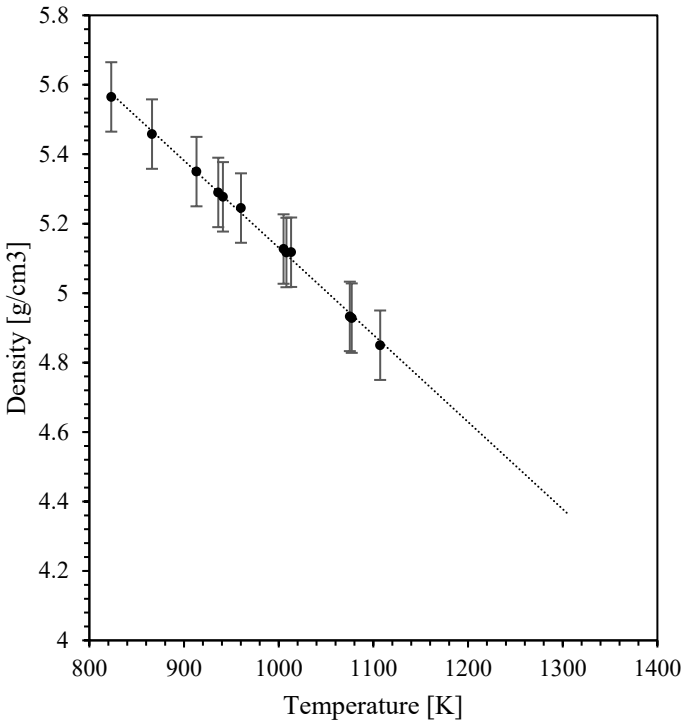

Table 5: Calculated density of $PuCl_3$ as a function of temperature. This data is derived from the density correlations summarized in *Table 4*.

Temperature [K]	Density [g/cm^3]
823	5.57
866	5.46
913	5.35
936	5.29
941	5.28
960	5.25
1005	5.13
1008	5.12
1013	5.12
1075	4.93
1077	4.93
1107	4.85

Figure 15: Calculated density of $PuCl_3$ as a function of temperature up to 1100 K, with extrapolation to 1300 K. Error bars represent 10% uncertainty. In the temperature range below the melt point of $PuCl_3$ ($T_m \approx 1040\ K$), the apparent density is only applicable above the liquidous temperature of multi-component systems containing $PuCl_3$.

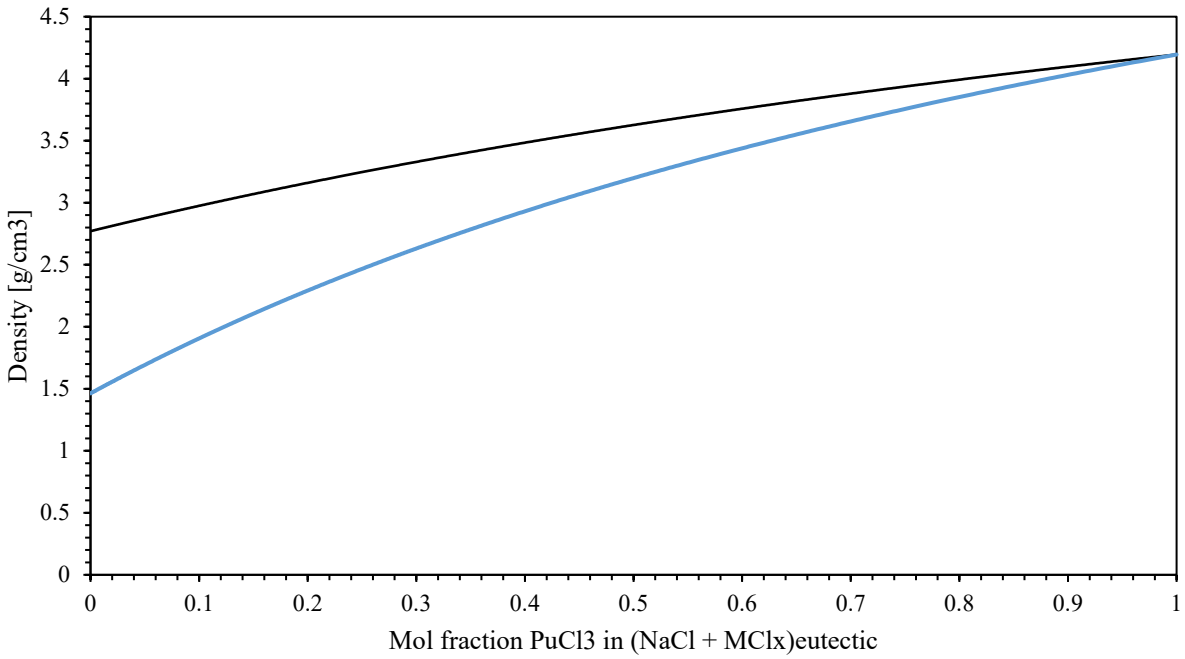

Figure 16: Calculated density of $PuCl_3$ in $(NaCl+MgCl_2)_{eutectic}$ (blue) and $(NaCl+UCl_3)_{eutectic}$ (black) mixtures as a function of mol fraction additions of $PuCl_3$, plotted at $T = 1100\ K$.

3.5 Discussion

The data shown in **Figures 13** and **14** represent all eight datasets. Duplicate samples are plotted together, with the dashed lines representing the average densities. A slight increase in UCl_3 and $PuCl_3$ concentrations in the NaCl + UCl_3 + $PuCl_3$ samples is associated with an apparent change in the coefficient of volumetric expansion. This is likely a contribution from the 2 mol% difference in UCl_3 concentration, as similar changes were observed in mixtures of {NaCl + UCl_3} [6]. This difference in the rate of expansion is not seen in the NaCl + $MgCl_2$ + $PuCl_3$ samples. The tight overlap across all duplicate pairs is an indication of the overall precision of the technique. The ternary systems examined in this work, {NaCl + $MgCl_2$ + $PuCl_3$} and {NaCl + UCl_3 + $PuCl_3$}, have been studied at least in preliminary, first-principle calculations of fundamental thermodynamic properties [14]. The range of applicability of the measured and calculated density data in this report is limited to the appropriate ternary liquid regions, which are shown in the ternary phase maps in **Figure 17**. The eutectic compositions of the binary mixtures are indicated by the intersection of the black lines with each axis, and the eutectic composition of the ternary mixture is shown as the intersection of three black lines. Using the $PuCl_3$ density correlation (**Figure 16**) derived from the density correlations given in **Table 4**, calculation of the density of $PuCl_3$ at arbitrary temperature in arbitrary mixtures of the corresponding eutectic solutions is possible by the derivation given in *Section 3.4*. This method of estimation requires the density correlation of the other individual components in the mixture, which have been measured and are reported in [6].

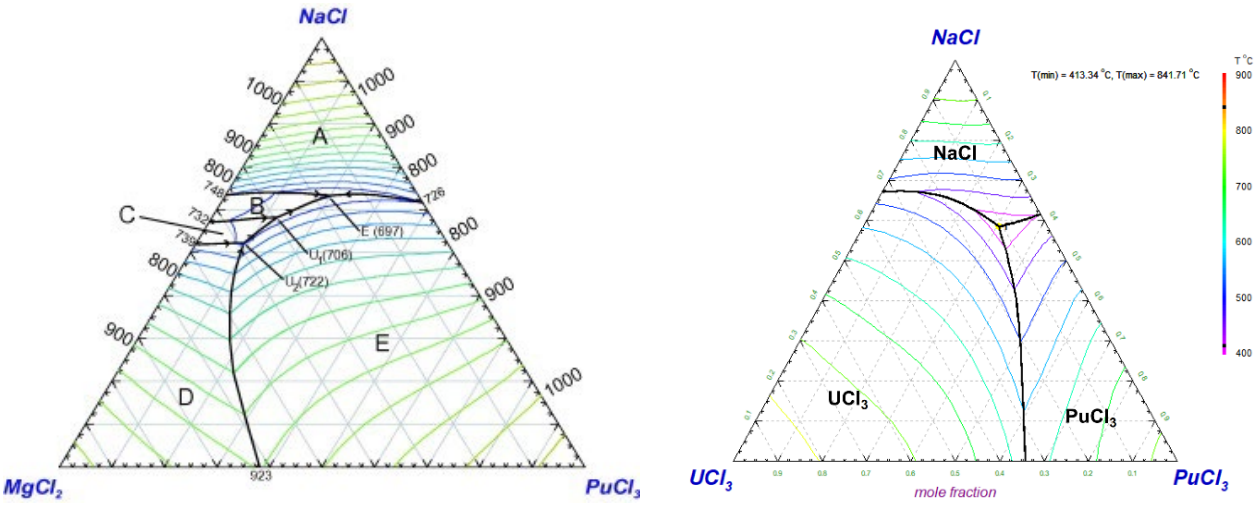

Figure 17: (*left*) Phase diagram of NaCl, $MgCl_2$, and $PuCl_3$ at the calculated eutectic temperature. [14] Liquidous temperatures are given in kelvin and are indicated on the plot and are illustrated across the phase space with colored contour lines. (*right*) Phase diagram of NaCl, UCl_3, and $PuCl_3$ at the calculated eutectic temperature. [15]. Liquidous temperatures are given in degrees Celsius and are indicated on the plot by the color heat map given on the right.

This method may be extended to include additional components, such as quaternary principle salts with minor inclusions of minor fission products. Calculation of the density as a function of $PuCl_3$ additions in eutectic mixtures (**Figure 17**) is a useful for bounding density due to the ingrowth of high-density species (e.g. transuranic) in the primary salt with an otherwise fixed relative composition. The anticipated uncertainty associated with these calculations will depend on the uncertainty of the density of the individual components, and the accuracy of the extrapolation necessary for $PuCl_3$ density data gathered below the melt point. Formation of oxide or oxychloride impurities in the $PuCl_3$ salts prior to use was not characterized. However, the formation of relatively small concentrations of these species would result in a significant increase in the density. Calculation of the density of salt mixtures from the pure components closely matched the measured densities of the salt mixtures, which suggests significant oxidation is not likely. Improvements to the accuracy of calculations described here will be accomplished by measurement of salt compositions with larger concentrations of $PuCl_3$ as well as higher temperature measurements. Measurements of the density of the binary eutectic solutions are high value, especially $(UCl_3 + PuCl_3)_{eutectic}$, as such data enable accurate estimation of the density of the ternary eutectics. These measurements also bound the lowest achievable density in that phase space.

4. Summary

The density of mixtures of {NaCl + $MgCl_2$ + $PuCl_3$} and {NaCl + UCl_3 + $PuCl_3$}, have been studied from melt to 1160 K. These measurements were accomplished through use of a specialized experimental setup optimized for high resolution neutron radiography. Given the ability to produce composite images of the entire sample change, aberrant features were identified and accounted for in the analysis of the data. The data from duplicate sample sets demonstrate a high degree of experimental precision. From the measured density correlations, a correlation for the density of $PuCl_3$ was derived. A method for the generalization of this data to extend to arbitrary mixtures was offered and show in the case of $PuCl_3$ additions in $(NaCl + MgCl_2)_{\textit{eutectic}}$ and $(NaCl + UCl_3)_{eutectic}$ mixtures. This work builds on previous studies of the density of liquid chlorides and forms the basis of future work measuring other intensive properties, such as viscosity. There remains potential to extract additional information with more advanced neutron imaging techniques: temperature and actinide density may be measured in-situ with neutron resonances, and material compositions can be measured with diffraction.

5. References

[1] T. Paget, J. McNeese, K. Fife, J. M. Jackson, R. Watson, Molten Salt Chemistry of Plutonium, LANL (2018).
[2] R. E. Thoma, Preparation, Purification, and Properties of the Uranium Chlorides: A Literature Survey, ORNL (1963).
[3] T. Lichtenstein, L. Gardner, M. A. Rose, Property Measurements of the NaCl-$PuCl_3$ Molten Salt System. ORNL (2020).
[4] C.W. Bjorklund, J.G. Reavis, J.A. Leary, K.A. Walsh J. Phys. Chem., 63 (10) pp. 1774-1777 (1959).
[5] T. Lichenstein, L. Gardner, M. A. Rose, ANL/CRCT-22/43 (2022).
[6] S. S. Parker, A. Long, C. Lhermitte, S. Vogel, M. Monreal, J. M. Jackson, J. Mol. Liq. 346, 118147 (2022)
[7] I. Barin, O. Knacke Thermochemical Properties of Inorganic Substances. Springer, Berlin, (1973).
[8] P. D. Myers, D. Y. Goswami, Appl. Therm. Eng. 109 p.889-900 (2016).
[9] A. S. Dworkin, M. A. Bredig, J. Phys. Chem. 64, 2 p.269–272 (1960).
[10] G. J. Janz, C. B. Allen, N. P. Bansal, R. M. Murphy, R. P. T. Tompkins, National Bureau of Standards NSRDS-NBS 61 Part 2 (1979).
[11] JANAF Thermochemical Tables, Michigan: U.S. Department of Commerce National Bureau of Standards / Institute for Applied Technology (1965-1968).
[12] B. Cardenas, N. Leon, Renewable Sustainable Energy Rev. 27 p.724-737 (2013).
[13] A. Kovacs, A. S. Booij, E. H. P. Cordfunke, S. A. Kok, R. J. M. Konings, J. Alloys Compd. 241 p.95-97 (1996).
[14] O. Benes, R.L.M. Konings J. Nucl. Mater. Vol 375 (2), pp 202-208 (2008).
[15] Molten Salt Thermal Properties Database-Thermochemical (*MSTDB-TC*), University of South Carolina (2023).